Kuwait J. Sci. **47 (3)** pp. 2-14, 2020

Meso research on the mechanical properties of rock specimens with double prefabricated circular holes based on digital image correlation

Wanhong Guo[1, 2, 3], Nengbin Chen[1], Yu Zhou[1]*, Li Wang[1, 3]

[1] *Key Laboratory of Ministry of Education for Efficient Mining and Safety of Metal Mine, University of Science and Technology Beijing, Beijing 100083, China*

[2] *Sinohydro Foundation Engineering Co., Ltd, Tianjin 301700, China*

[3] *PowerChina Road Bridge Group Co., Ltd., Beijing 100048, China*

** Corresponding author: westboy85@sina.com.cn.*

Abstract

Based on digital image correlation (DIC) and acoustic emission (AE) technology, combined with particle flow theory and particle follow code (PFC) program, the crack propagation law of rock samples with double pre-existing holes under uniaxial compression and the damage and failure process of rocks were studied systematically. The main findings are as follows: (1) In the early stages of the test loading, as the load increases, it can be found from the evolution of the cloud diagrams that the strain is transferred from the initial distribution around the prefabricated circular holes to the upper and lower ends of the prefabricated circular holes, and gradually extends outward along the vertical direction. (2) During the period from the stable expansion phase of the crack to the nonstable expansion phase, a sharp increase in the number of acoustic emission events accompanies the stress-strain curve when it has a stress drop. In addition, the greater the absolute value of the stress drop, the greater the frequency of acoustic emission events. (3) Obvious "anti-symmetric" features are exhibited in both the horizontal and vertical displacement fields; the displacement of the vertical displacement field is distributed in a V-shape upward and downward at the center of the round hole, respectively. (4) The DIC technique can be used to quantitatively describe the evolution of the crack displacement field and strain field in the process of rock failure, providing a more intuitive and accurate way for the study of crack evolution.

Key words: Crack propagation; digital image correlation; particle flow code; rock mechanics; uniaxial compression.

1. Introduction

Because of long-term geological structure and human activities, rocks in the natural conditions often have a large number of defects such as microcracks and holes. Under the action of loading, the cracking, propagation and coalescence of these defects are the main manifestations of the instability and destruction of the material of rocks. Therefore, it is of great practical value and theoretical significance to study the mechanism of cracks and crack evolution in rocks containing holes. The goal is to gain understanding of geotechnical engineering geo-hazards so that corresponding measures can be taken for mitigation.

2. Literature review

Bobet & Einstein (1998) carried out a large number of uniaxial laboratory compression tests. The research investigated three kinds of tensile crack propagation modes, three kinds of shear crack propagation modes, and one kind of tensile-shear mixed crack propagation mode. Wong & Einstein (2009a; 2009b) used high-speed photography and scanning electron microscopy to study the macro-mechanism and rule of crack initiation, propagation, and the coalescence of gypsum and marble under uniaxial compression. Yang *et al*. (2012) and Yang (2014) analyzed the effect of rock bridge inclination on the strength of sandstone specimens by prefabricating three cracks in sandstone. The studies examined the crack propagation mechanism of sandstone specimens under uniaxial compression. Young *et al*. (2000) and Thompson *et al*. (2006) studied the intrinsic mechanism of acoustic emission events in the initial microcrack propagation of rocks through acoustic emission localization. Meglis *et al*. (1995) used acoustic emission technology to study the temporal and spatial evolution of microcracks in the vicinity of rock holes. Zhang & Wong (2012; 2013) and

Zhang *et al*. (2015) used the PFC program to study the propagation of cracks in a single fractured rock mass under uniaxial compression. Zhou *et al*. (2014), Zhou *et al*. (2018a), Zhou *et al*. (2018b), Li *et al*. (2019), Zhou *et al*. (2019) and Wu *et al*. (2020) made a quantitative study of the mechanical properties of rock masses from the perspective of meso-mechanics based on the PFC procedure. Finally, Digital image correlation (DIC) was proposed in the early 1980s. Peters (1982) and Yamaguchi (2000) applied this method to the deformation analysis of rock damage.

In this paper, through using digital image correlation and acoustic emission technology combined with PFC program, we construct rock samples containing circular holes to study the mechanical properties and the evolution law of cracks of the sample under uniaxial compression and reveal the meso-mechanism of the fracture pattern of rock samples.

3. Research methods

3.1 Digital image correlation

As shown in Figure 1, digital image correlation is a non-contact full-field measurement technique that acquires parameters such as displacement and deformation of the object by correlating the processing of two images on the surface of an object before and after deformation. When all photos are taken into the analysis system, parameters can be achieved such as the displacement field, incremental displacement field, strain field and strain rate of change, according to the deformation images observed at different times.

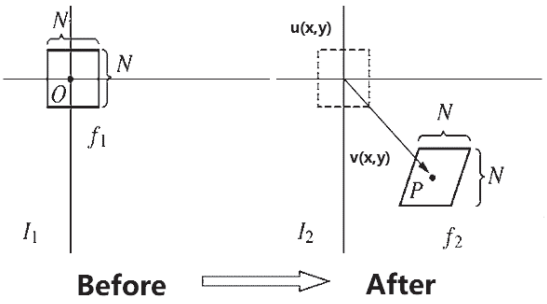

Fig. 1 Sketches of correlation match

3.2 Simulation methods

The particle flow theory and PFC program use the discrete element method to simulate the motion and interaction of circular granular media. The contact point between the particles of the parallel bonding model has the ability to resist bending deformation, which can truly reflect the mechanical properties of the sample. Therefore, the parallel bonding model was used for this study.

Reasonable meso-parameters are paramount to numerical simulations. Through multiple trial adjustments, the simulation results were consistent with the test results. The meso-mechanical parameters of the particles are shown in Table 1.

Table 1. Meso mechanical parameters of bonded particle model

Particle					
Minimum particle radius R_{min}/mm	Particle radius ratio Rrat	Bulk density ρ/(kg·m^{-3})	Friction coefficient μ	Young's modulus Ec/GPa	Stiffness ratio of normal and shear $\overline{k}_n/\overline{k}_s$
0.24	1.66	2100	1	3.80	3.1

Parallel bonding model						
Young's modulus $\overline{E}_c$/GPa	Stiffness ratio of normal and shear $\overline{k}_n/\overline{k}_s$	Friction coefficient $\overline{\mu}$	Bond tensile strength σ_b/MPa	Standard deviation of bond tensile strength /MPa	Bond cohesion c_b/MPa	Standard deviation of bond cohesion /MPa
3.80	3.1	1	25.0	2.50	25.0	2.50

4. Sample materials and experimental process

4.1 Test preparation

Various random defects exist in natural rocks, and they have a great impact on rock failure morphology. In order to eliminate the effect of random defects on the specimen, this article uses a high-strength cement-like rock material to make specimens. The size of the test specimen was 50 mm × 50 mm × 100 mm. The diameters of the two prefabricated circular holes were both 10 mm. The center point of the circular hole was 20 mm from the horizontal direction of the sample centroid, and the vertical distance was 10 mm. In addition, the two prefabricating circular holes were symmetrically distributed along the centroid of the sample. Figure 2(a) shows the geometry of the prefabricated circular holes.

Since the test required the use of acoustic emission and digital image (DIC) technology, before it could be carried out, a silica gel was used as a coupling agent to bond the acoustic emission detector and the sample. As shown in Figure 2(b), white paint was sprayed on the observation surface of the sample, and after the coating dried, black particles were randomly applied to form a random speckle. The black paint was sprayed so that the paint particles were as uniform as possible, allowing for good recognition during image processing.

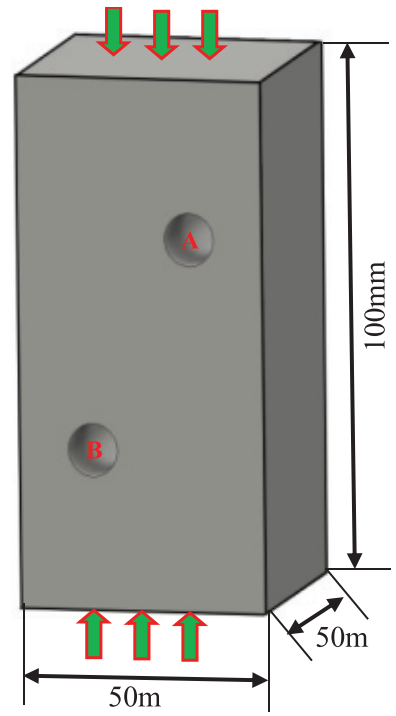

(a) Geometry of specimen

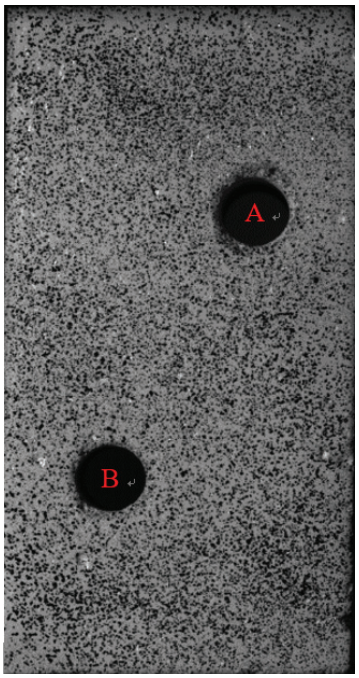

(b) Speckle pattern of specimen

Fig. 2. Illustration of specimen pattern

4.2 Test equipment and process

The test system consisted of a loading, observation, data analysis, and acoustic emission monitoring systems (Figure 3). The loading system used a YAW-600 microcomputer controlled electro-hydraulic servo rock tester. The observation system consisted of a light emitting diode (LED) lamp and a set of shooting devices. The LED lamp provided a stable light source for the test so as to match the image obtained by the shooting device with a stable gray value. The acquisition rate of the high-speed camera was adjusted according to the preset loading rate. The analysis system used the Vic-2D software from Correlated Solutions from the United States. During the test, the acoustic emission technology was used to monitor the spatial evolution patterns of microcrack initiation and propagation. The test acoustic emission monitoring system adopted the IMaGE acoustic emission monitoring system produced by Itasca company in the United States. The number of channels was 8, and the sampling frequency was 5 MHz.

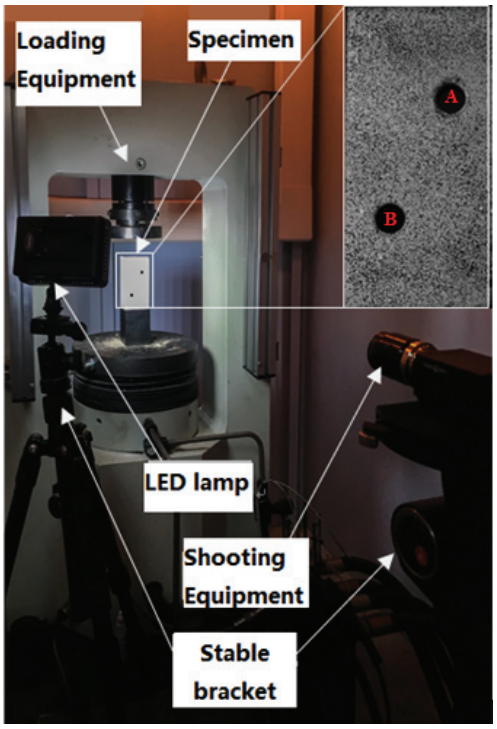

Fig. 3. Experimental setup

5. Testing and calculation of results and analysis

5.1 Effect of prefabricated circular holes on strength

In Figure 4, (a) is the variation law of the acoustic emission event with the stress-strain curve, and (b) is the variation rule of the number of micro-ruptures with the stress-strain curve. According to Figure 4(a), the peak strength of the test specimen was about 25.2 MPa, the corresponding strain was about 6.9×10^{-3}, and the pre-peak elastic modulus was approximately 6.4 GPa. Before the compressive strength of the specimen reached its peak strength, the stress-strain curve showed a nearly linear upward trend with a smaller stress drop in the middle. The starting point of the unstable stage of crack propagation occurred when the stress-strain curve reached its peak. After the peak, the slope of the corresponding stress-strain curve increased sharply with three large stress drops. The three stress drops were relatively severe. The peak strength of the sample obtained by numerical simulation was about 26.6 MPa, the corresponding strain equaled about 6.9×10^{-3}, and the pre-peak elastic modulus was about 4.7 GPa. However, since the particles in the constructed model were all in close contact, and there were no particles with a contact number of less than 3, the pre-peak phase of the stress-strain curve then increased approximately linearly. After the peak, the stress-strain curve had an approximately linear downward trend. Compared to the experimental stress-strain curve, the stress-strain curve obtained by numerical simulation was generally similar, the location and value of the stress peak were basically the same, and the location of the failure point was also basically the same.

From Figure 4(a), it can be seen that the total number of acoustic emission events obtained during the test was 2117 times. In the early stage of loading (that is, before the strain was 2.8×10^{-3}), there were fewer acoustic emission events, but the number of times was less. As the load increased, the number of acoustic emissions started to increase gradually, which means that the larger-scale micro-ruptures in the sample began to increase. Before the peak, the relationship between the number of acoustic emission events and the strain was similar to the stress-strain relationship. In other words, the stress-strain relationship had a similar relationship to the number of acoustic emission events and the strain. After peak intensity, the acoustic emission event was more active. A sharp increase in the number of acoustic emission events accompanied the stress-strain curve when it had a stress drop. In addition, the greater the absolute value of the stress drop was, the greater the frequency of the acoustic emission events was.

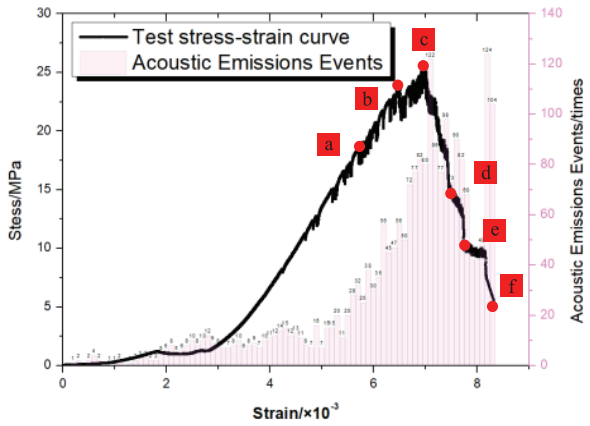

(a) Change of acoustic emission events with test stress-strain curve

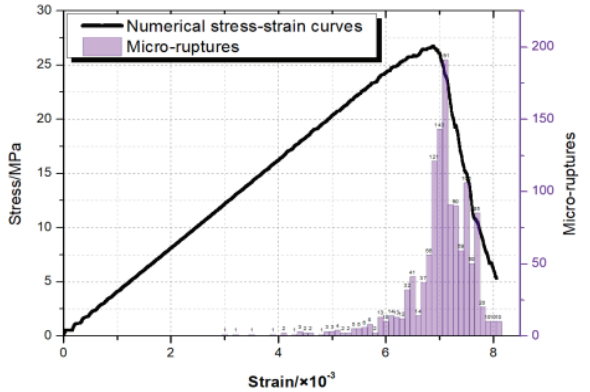

(b) Changes in micro-rupture with stress-strain curve of numerical simulation

Fig. 4. Loading stress-strain curve

The total number of micro-ruptures obtained in the numerical simulation was 1286 (Figure 4 (b)). Before peak intensity, among them, the number of microcracks was less (total number of microcracks = 298), accounting for about 23.1% of them. After peak intensity, the micro-rupture became very active (total number of microcracks = 988), accounting for approximately 76.8%.

In general, the stress-strain curve of the sample obtained by the numerical simulation is consistent with the test results.

5.2 Influence of prefabricated circular holes on crack propagation

Figure 5 represents full-field strain cloud diagrams at different times during the test. Figure 4 (a) shows the corresponding stress-strain state. The diagrams show that the macroscopic cracks generated during the failure of the sample can be divided into two categories. The first is an I-type crack (also called a tensile crack) which usually has a relatively slender width and develops in the direction of loading. The other type is a II-type crack (or shear crack) which has a generally wider width and develops at an angle to the loading direction. In addition, the changes shown in the diagrams demonstrate the characteristics of the entire rock damage process. This fully reflects the evolution trend of the high-strain region of the sample.

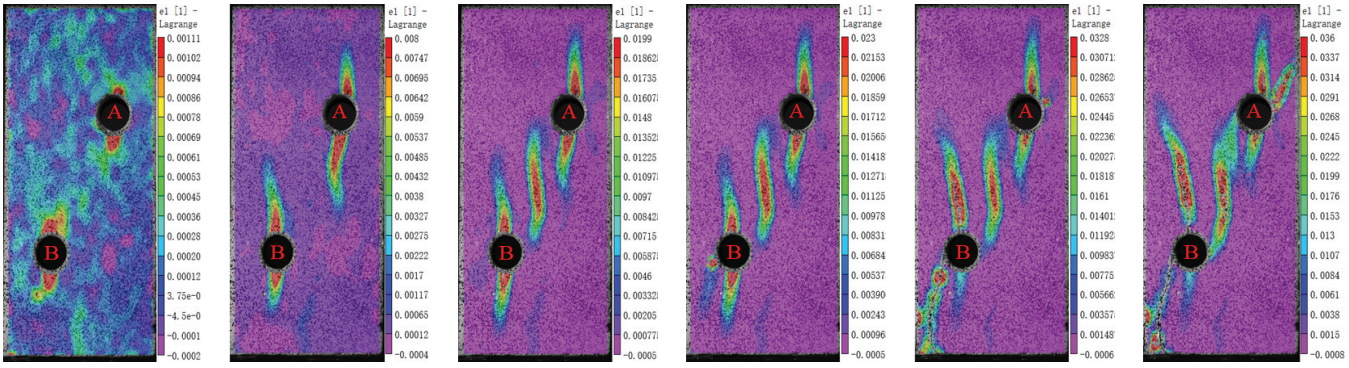

(a) point **a** (b) point **b** (c) point **c** (d) point **d** (e) point **e** (f) point **f**

Fig. 5. Full-field strain cloud diagrams

(**a.** ε=5.8×10^{-3}, σ=18.5MPa; **b.** ε=6.4×10^{-3}, σ=24.0MPa; **c.** ε=6.9×10^{-3}, σ=25.5MPa; **d.** ε=7.5×10^{-3}, σ=15.0MPa; **e.** ε=7.8×10^{-3}, σ=10.0MPa; **f.** ε=8.2×10^{-3}, σ=5.0MPa)

As shown in Figure 5(a), when the experimental stress-strain curve reached point **a**, the strain field change was basically concentrated near the prefabricated circular hole, and the maximum strain occurred at the upper and lower ends of the prefabricated circular hole. However, no obvious new cracks appeared on the observed surface of the sample.

As the load continued to increase, the experimental stress-strain curve reached point **b**. The figures show that the strain field was transferred from the initial distribution around the prefabricated circular hole to the upper and lower ends of the prefabricated circular hole. The strain field and gradually extended outward along the vertical direction. This indicates that the I-type crack was in a rapid expansion phase.

Figure 5(c) shows that when the stress reached the peak strength point **c**, the area of strain concentration appeared in the rock bridge areas of the two prefabricated circular holes, but there was no connection. In addition, at this stage, the stress-strain curve fluctuated up and down. The phenomenon shows the origination and expansion of II-type cracks at this stage cause stress redistribution in the specimen and changes in the compressive structure, which led to an unstable growth of stress and strain. In other words, the outcome is a phenomenon in which the curve fluctuated up and down.

When the test stress-strain curve reached point **d**, the crack changed from the stable expansion phase of the early stage to the nonstable expansion phase. Observing

the stress-strain curve, it was obvious that there was a relatively long duration, and the large amplitude stress dropped at this stage. The strain concentration area in the rock bridge area gradually bent and approached the prefabricated circular holes. The high-strain concentrated area began to appear at the bottom left of the prefabricated circular hole **B**. Although the strain value was low, it could still predict the development trend of the strain area to some extent.

When the test stress-strain curve reached point **e**, the II-type crack between the outside of the circular hole B and the sample boundary was completely penetrated. At this stage, the stress-strain curve dropped sharply, and the rock bridge area of the two pre-fabricated round holes were basically penetrated. The strain concentration area begins to appear at the right upper end of the preformed circular hole **A**.

When the test stress-strain curve reached point **f**, the test was completed with the last stress drop. The II-type cracks between the outside of the prefabricated circular hole **A** and the boundary of the sample were completely penetrated, and the entire sample was destroyed.

Figure 6 shows the micro-rupture propagation process obtained by numerical simulation. Figure 4(b) has the corresponding stress-strain states marked. Using the Crk-item in the PFC, the micro-rupture propagation could be effectively tracked during loading. The red short lines in the figures represent tensile micro-ruptures, and the black short lines are shear micro-ruptures.

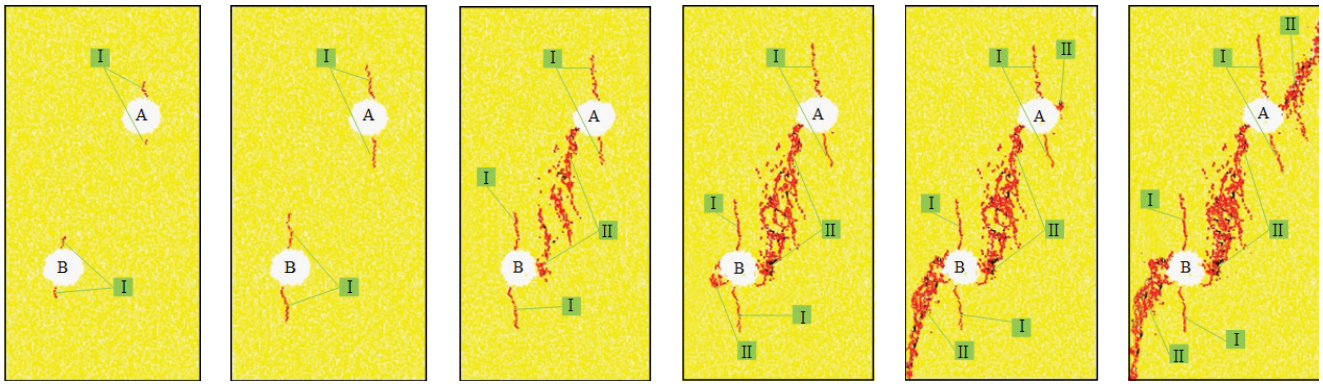

(a) point **a′** (b) point **b′** (c) point **c′** (d) point **d′** (e) point **e′** (f) point **f′**

Fig. 6. Micro-ruptures evolution of numerical simulation

(**a′.** ε=5.8×10^{-3}, σ=24.0MPa; **b′.** ε=6.4×10^{-3}, σ=25.5MPa; **c** ε=6.9×10^{-3}, σ=26.6MPa; **d′.** ε=7.4×10^{-3}, σ=17.0MPa; **e′.** ε=7.8×10^{-3}, σ=10.0MPa; **f′.** ε=8.2×10^{-3}, σ=5.0MPa)

Before peak intensity, when the stress-strain curve reached point **a′**, the micro-ruptures were first generated at the upper and lower ends of the prefabricated circular holes **A** and **B** and formed an initial I-type crack.

When the stress-strain curve reached point **b′**, the I-type cracks at the upper and lower ends of the prefabricated circular holes **A** and **B** further expanded, micro-ruptures gradually increased, and the direction was gradually parallel to the direction of the maximum principal stress.

When the stress-strain curve reached point **c′**, the micro-ruptures forming the II-type crack began to develop and expand between the two prefabricated circular holes.

After peak intensity, when the stress-strain curve reached point **d′**, the II-type crack between the lower end of circular hole **A** and the upper end of the circular hole **B** were completely penetrated. At this point, the rock bridge between the two prefabricated circular holes was penetrated, and the micro-ruptures that formed the II-type crack at the lower left end of circular hole **B** started to form.

When the stress-strain curve reached point **e′**, the II-type crack between the lower end of circular hole **B** and the sample boundary was completely penetrated, and the micro-ruptures of the II-type crack at the upper right end of circular hole **A** started to form. It should be noted that the I-type cracks at the upper and lower ends of the prefabricated circular holes developed slowly or even stopped at this stage of the experiment.

When the stress-strain curve reached point **f′**, the II-type crack completely connected between the upper

right end of circular hole **A** and the sample boundary. At this point, the sample was completely destroyed. In general, the characteristics of crack evolution at each stage of the test and the numerical simulation were consistent.

5.3 Effect of prefabricated circular holes on evolution of displacement field

In order to more fully understand crack initiation, propagation, penetration, and rock damage characteristics from a mesoscopic point of view, the evolution of the sample's full-field displacement cloud diagrams can be analyzed. Figure 7 represents full-field displacement cloud diagrams of the ***X*** direction (horizontal direction) at different points during the test. Figure 4(a) has marked its corresponding stress-strain state has been marked in. The full-field displacement cloud diagrams of the ***X*** direction exhibited the character of "anti-symmetry". With the increase of the load, the displacement at the left end of two prefabricated circular holes was negative, the displacement at the right end was positive, and the absolute value of displacement gradually increased. In addition, there was a clear demarcation line between the different displacement areas found in the full-field displacement cloud diagrams in the ***X*** direction. The demarcation line is the path for the initiation and propagation of I-type cracks during sample loading (see Figure 5).

Figure 8 is a full-field displacement cloud diagrams of the ***Y*** direction (Vertical direction) at different times during the test. Figure 4(a) shows the corresponding stress-strain state marks. The full-field displacement cloud diagrams of the ***Y*** direction represent the character of "anti-symmetrical" in the figure. From the observation point **a** to **d**, the displacement in the ***Y*** direction gradually increased with load increase. The displacement of the upper end of the preformed circular hole **A** and the lower end of the prefabricated circular hole **B** were distributed in a V-shape upward and downward at the center of the round hole, respectively. From the observation point **e** to **f**, the displacement area of the left and right sides of the prefabricated circular holes had a clear demarcation line. Figure 5 shows that this demarcation line is the path of II-type crack propagation, or the location of the final macroscopic crack of the specimen.

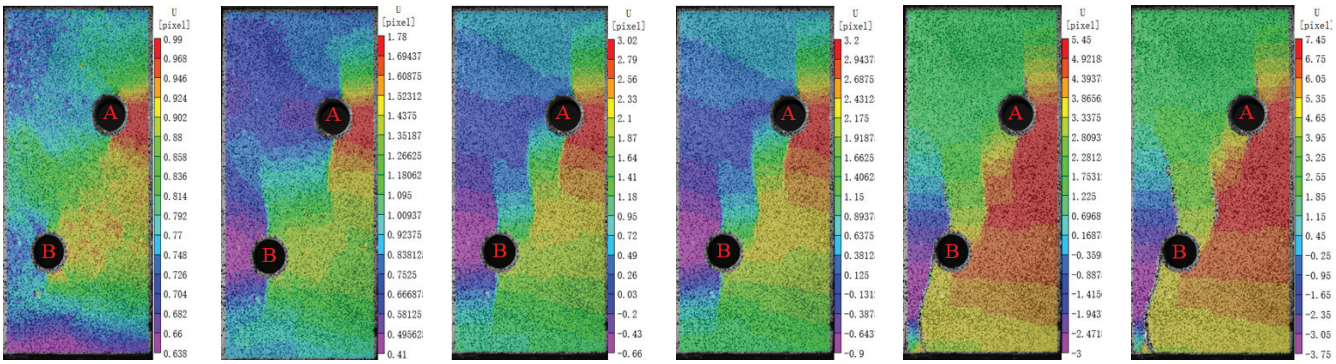

(a) point **a** (b) point **b** (c) point **c** (d) point **d** (e) point **e** (f) point **f**

Fig. 7. Full-field displacement cloud diagrams of the *X* direction

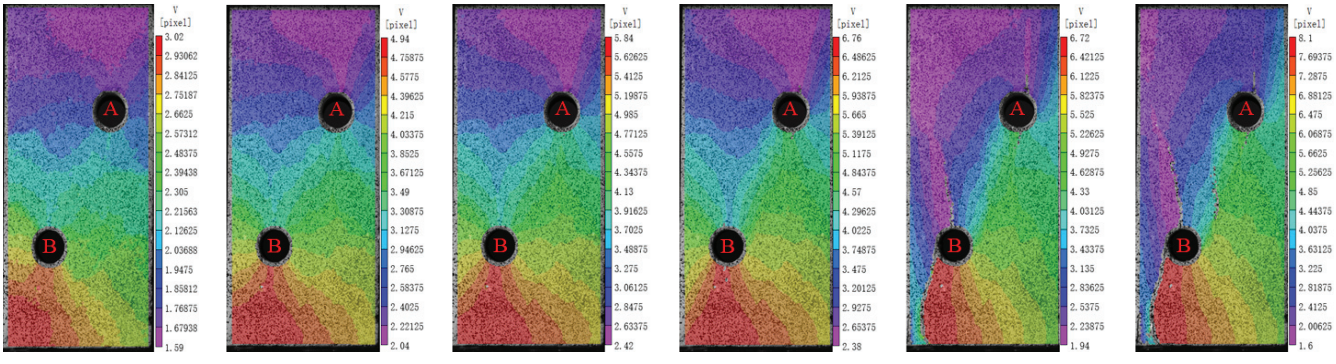

(a) point **a** (b) point **b** (c) point **c** (d) point **d** (e) point **e** (f) point **f**

Fig. 8. Full-field displacement cloud diagrams of the *Y* direction

6. Conclusion

Based on digital image correlation technology (DIC) and acoustic emission technology, combined with particle flow theory and PFC program, the uniaxial compression test of the sample was conducted to study the evolution rules and distribution patterns of crack initiation during failure of the specimen in this article. The main findings are as follows:

(1) In the early stages of the test loading, as the load increased, the evolution of the cloud diagrams show that strain was transferred from the initial distribution around the prefabricated circular holes to the upper and lower ends of the prefabricated circular holes. It then gradually extended outward along the vertical direction.

(2) During the period from the stable expansion phase of the crack to the nonstable expansion phase (when the stress-strain curve had a stress drop) it was accompanied by a sharp increase in the number of acoustic emission events. In addition, the greater the absolute value of the stress drop was, the greater the frequency was of acoustic emission events.

(3) Of the two groups of full-field displacement cloud diagrams, it was concluded that:

- The full-field displacement cloud diagrams of ***X*** and ***Y*** directions both exhibit obvious "anti-symmetric" features; and
- In the full-field displacement cloud diagrams of the ***Y*** direction, the displacement of the upper end of the preformed circular hole **A** and the lower end of the prefabricated circular hole **B** were distributed in a V-shape upward and downward at the center of the round hole, respectively.

(4) The DIC technique can be used to quantitatively describe the evolution of crack displacement and strain fields in the process of rock failure, providing a more intuitive and accurate way to study crack evolution.

ACKNOWLEDGEMENTS

This research was supported by the Fundamental Research Funds for the Central Universities (Grant No. FRF-TP-18-016A3).

Reference

Bobet, A. & Einstein, H.H. (1998). Fracture coalescence in rock-type materials under uniaxial and biaxial compression. International Journal of Rock Mechanics & Mining Sciences, **35**(7): 863-888.

Li, J. W., Zhou, Y., Sun, W. & Sun, Z. (2019). Effect of the interaction between cavity and flaw on the rock mechanical property under uniaxial compression. Advances in Materials Science and Engineering, Article ID 1242141.

Meglis, I.L., Chows, T.M. & Young, R.P. (1995). Progressive microcrack development in tests in Lac du Bonnet granite—I. Acoustic emission source location and velocity measurements. International Journal of Rock Mechanics & Mining Sciences & Geomechanics Abstracts, **32**(8): 741-750.

Peters, W.H. (1982). Digital image techniques in experimental stress analysis. Optical Engineering, 21.

Thompson, B.D., Young, R.P. & Lockner, D.A. (2006). Fracture in westerly granite under AE feedback and constant strain rate loading: Nucleation, quasi-static propagation, and the transition to unstable fracture propagation. Pure & Applied Geophysics, **163**(5): 995-1019.

Wong, L.N.Y. & Einstein, H.H. (2009a). Crack coalescence in molded gypsum and Carrara marble: Part 1. Macroscopic observations and interpretation. Rock Mechanics & Rock Engineering, **42**(3): 475-511.

Wong, L.N.Y. & Einstein, H.H. (2009b). Crack coalescence in molded gypsum and Carrara marble: Part 2. Microscopic observations and interpretation. Rock Mechanics & Rock Engineering, **42**(3): 513-545.

Wu, T.H., Gao, Y.T., Zhou, Y. & Li, J.W. (2020). Experimental and numerical study on the interaction between holes and fissures in rock-like materials under uniaxial compression. Theoretical and Applied Fracture Mechanics, **106**: 102488.

Yamaguchi, I. (2000). A laser-speckle strain gauge. Journal of Physics E: Scientific Instruments, **14**(11): 1270.

Yang, S.Q., Yang, D.S., Jing, H.W., Li, Y.H. & Wang, S.Y. (2012). An experimental study of the fracture coalescence behaviour of brittle sandstone specimens containing three fissures. Rock Mechanics & Rock Engineering, **45**(4): 563-582.

Yang, S.Q. (2014). Discrete element modeling on fracture coalescence behavior of red sandstone containing two unparallel fissures. Engineering Geology, **178**: 28-48.

Young, R.P., Hazzard, J.F. & Pettitt, W.S. (2000). Seismic and micromechanical studies of rock fracture. Geophysical Research Letters, **27**(12): 1767-1770.

Zhang, X.P. & Wong, L.N.Y. (2012). Cracking processes in rock-like material containing a single flaw under uniaxial compression: A numerical study based on parallel bonded-particle model approach. Rock Mechanics & Rock Engineering, **45**(5): 711-737.

Zhang, X.P. & Wong, L.N.Y. (2013). Loading rate effects on cracking behavior of flaw-contained specimens under uniaxial compression. International Journal of Fracture, **180**(1): 93-110.

Zhang, X.P., Liu, Q.S., Wu, S.C. & Tang, X. (2015). Crack coalescence between two non-parallel flaws in rock-like material under uniaxial compression. Engineering Geology, **199**: 74-90.

Zhou, J.X., Zhou, Y. & Gao, Y.T. (2018a). Effect mechanism of fractures on the mechanics characteristics of jointed rock mass under compression. Arabian Journal for Science and Engineering, **43**: 3659-3671.

Zhou, Y., Wu, S.C., Gao, Y.T. & Misra, A. (2014). Macro and meso analysis of jointed rock mass triaxial compression test by using equivalent rock mass (ERM) technique. Journal of Central South University of Technology, **21**(3): 1125-1135.

Zhou, Y., Zhang, G., Wu, S.C. & Zhang, L. (2018b). The effect of flaw on rock mechanical properties under the Brazilian test. Kuwait Journal of Science, **45**(2): 94-103.

Zhou, Y., Chen, N.B., Wang, L. & Wu, T.H. (2019). A flat-joint contact model and meso analysis on mechanical characteristics of brittle rock. Kuwait Journal of Science, **46**(3): 71-82.

Submitted: 28/10/2018
Revised: 29/11/2018
Accepted: 02/12/2018

بحث وسيط عن الخواص الميكانيكية لعينات صخرية ذات ثقوب دائرية مزدوجة جاهزة التركيب على أساس مضاهاة الصور الرقمية

وانهونج جو، [1]ننجبن تشن ، *[1]يو زو [3،1]لي وانق [3،2،1]

westboy85@sina.com.cn

ملخص

يوضح هذا البحث بعد دراسة منهجية معتمدة على مضاهاة الصور الرقمية (DIC) وتكنولوجيا الانبعاث الصوتي (AE) المُدمجة مع نظرية تدفق الجُزيء وبرنامج كود تدفق الجُزيء (PFC)، واتساع التصدعات حسب قانون عينات الصخور ذات الثقوب المزدوجة والموجودة بالفعل تحت ضغط أحادي المحور وعمليات تلف وضعف الصخور، توصلت النتائج الرئيسية للبحث إلى: (1) يتضح في المراحل الأولى من تحميل الاختبار، أنه كلما زادت الحمولة، تمكننا من خلال تتبع تطور الرسم البياني السحابي اكتشاف تحول الالتواء من التوزيع المبدئي حول الثقوب الدائرية إلى الانتشار حول الأطراف السفلى والعليا للثقوب الدائرية جاهزة التركيب، والتي تمتد تدريجياً نحو الخارج وتتخذ اتجاهاً عمودياً. (2) اثناء الفترة ما بين مرحلة التمدد المُستقر للصدع إلى مرحلة التمدد غير المستقر، تحدث زيادة حادة في عدد أحداث الانبعاث الصوتي وتكون مصحوبة بتقوس الالتواء عند حدوث هبوط في الجهد. وعلاوة على ذلك، كلما زادت القيمة المُطلقة لهبوط الجهد، زاد تكرار أحداث الانبعاث الصوتي. (3) تظهر الملامح الواضحة غير المتماثلة في مجال الانزياح العمودي والممتد على شكل حرف V أعلى وأسفل مركز الثقب الدائري على التوالي. (4) يمكن استخدام تقنية ال DIC بشكل كمي لوصف تطور مجال انزياح الصدع ومجال الالتواء في عمليات القصور الصخري، مما يمثل طريقة أكثر دقة وبداهة لدراسة تطور الصخور.